1 **Physical mechanisms for biological carbon uptake during the onset of the spring**

2 **phytoplankton bloom in the northwestern Mediterranean Sea (BOUSSOLE site)**

3 Liliane Merlivat[1], Michael Hemming [2], Jacqueline Boutin[1], David Antoine[3, 4], Vincenzo

4 Vellucci[5], Melek Golbol[5], Gareth A. Lee[6], Laurence Beaumont[7]

5 [1] Sorbonne Université, CNRS/IRD/MNHN, LOCEAN, IPSL, Paris, France

6 [2] Coastal and Regional Oceanography Lab, Centre for Marine Science and Innovation, UNSW

7 Sydney, Sydney, NSW 2052 Australia

8 [3] Remote Sensing and Satellite Research Group, School of Earth and Planetary Sciences,

9 Curtin University, Perth, WA 6845, Australia

10 [4] Sorbonne Université, CNRS, Laboratoire d'Océanographie de Villefranche, Villefranche sur

11 Mer 06230, France

12 [5] Sorbonne Université, CNRS, Institut de la Mer de Villefranche, Villefranche sur Mer 06230,

13 France

14 [6] Centre for Ocean and Atmospheric Sciences, School of Environmental Sciences, University

15 of East Anglia, Norwich Research Park, Norwich NR4 7TJ, UK

16 [7] Division Technique INSU-CNRS, 92195 Meudon CEDEX, France

18 Correspondence to: liliane.merlivat@gmail.com

19 Keywords: Bloom onset ; Carbon uptake ; Air-sea interaction; Mediterranean sea

20 Abstract

21 Several trigger mechanisms have been proposed for the onset of the phytoplankton spring

22 bloom. Among these, that phytoplankton cells begin to bloom when they experience higher

23 average light levels in shallower mixed layers, a result of the surface net heat fluxes becoming

24 positive and wind strength decreasing. We study the impact of these two forcings in the

25 northwestern Mediterranean Sea. We take advantage of hourly measurements of oceanic and

26 atmospheric parameters collected at two neighboring moorings during the months of March

27 and April in the years 2016 to 2019, combined with glider data in 2016. The onset of the

28 surface phytoplankton growth is concomitant with the start of significant biological activity
29 detected by a sudden decrease in dissolved inorganic concentrations derived from
30 measurements in the upper 10 m of the water column. A rapid reduction in wind stress
31 following high-wind events is observed at the same time. A resulting shallow mixing layer
32 favors carbon uptake by phytoplankton lasting a few days. Simultaneously, the air-sea net
33 heat flux switches from negative to positive linked to changes of the latent air-sea heat flux,
34 which is proportional to the wind speed. This results in an increased thermal stratification of
35 the ocean's surface layers. In 2016, glider data show that the mixing layer is significantly
36 shallower than the mixed layer at the onset of the surface phytoplankton bloom. We conclude
37 that decreases in the mixing and mixed layer depths lead to the onset of the phytoplankton
38 bloom due to the relaxation of wind speed following storms. We estimate net daily
39 community production in the mixing layer over periods of 3 days between 2016 and 2019 as
40 between 38 mmol C m^{-2} and 191 mmol C m^{-2}. These results have important implications as
41 biological processes play a major role in the seasonal evolution of surface pCO2 and thereby
42 the rate of reduction of atmospheric CO_2 by exchange at the air-sea interface.

43

44

45

46 Introduction

47 Investigating the physical and biological mechanisms contributing to changes in air-sea
48 carbon dioxide (CO_2) fluxes is essential. It is a critical component of the global carbon cycle
49 and the climate system with the ocean removing about a quarter of the CO_2 emitted into the
50 atmosphere by human activities over the last decade. It depends on the gradient of CO_2 partial
51 pressure, pCO$_2$, between the atmosphere and the surface ocean [Takahashi et al., 2009;
52 Rödenbeck et al., 2013; Merlivat et al., 2015]. pCO$_2$ in the ocean mixed surface layer
53 depends on the relative contribution of dynamic transport, thermodynamics and
54 biogeochemistry. As the biological carbon pump lowers pCO$_2$ and Dissolved Inorganic
55 Carbon (DIC) at the sea surface, the production of plankton biomass during a bloom can be
56 sufficient to reverse the annual cycle of surface-ocean CO_2 uptake. A decrease in surface DIC,
57 after physical processes have been eliminated, indicates the beginning of phytoplankton
58 spring growth. Conceptual frameworks have been proposed to explain when depth-integrated

59   phytoplankton biomass starts accumulating during blooms [Behrenfeld, 2010; Sverdrup,
60   1953]. The timing of the initiation of the surface spring phytoplankton bloom depends in
61   particular on atmospheric forcing. The physical processes of wind stress, heat flux and
62   vertical mixing control the depth of the mixed/mixing layer and thus the availability of light
63   [Siegel et al, 2002, Chiswell, 2011; Taylor and Ferrari, 2011; Brody and Lozier, 2015;
64   Enriquez and Taylor, 2015, Rumyantseva et al, 2019].   Thus, to better understand which
65   fundamental physical processes control the timing of the onset of the surface bloom, in situ
66   measurements are needed at the appropriate hourly to daily timescale. It is important to draw
67   attention to the atmospheric forcing timescale. In biogeochemical ocean modeling studies,
68   typically built on atmospheric models, reanalysis or satellite data, time resolution of at best a
69   few days are required [Mahadevan et al, 2012].
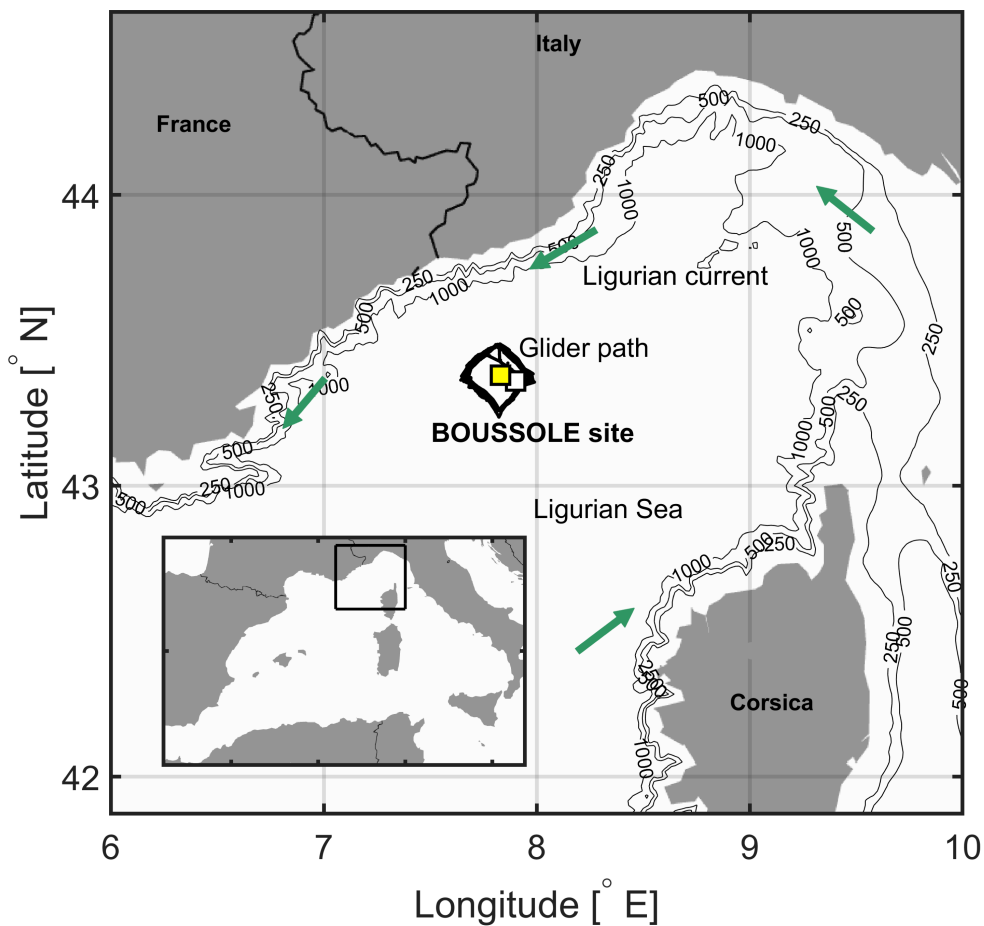
70

71   Figure 1. The area of the northwestern Mediterranean Sea showing the French and Italian
72   Rivieras, the island of Corsica, the main current branches (green arrows) in the Ligurian Sea
73   and the location of the BOUSSOLE buoy (white square) and the AZUR meteorological buoy
74   (yellow square). The black line indicates the glider's path in March-April 2016.

75   In the northwestern Mediterranean Sea, the BOUSSOLE (Bouée pour l'acquisition de Séries

76   Optiques à Long Terme; Antoine et al., 2006, 2008a,b) buoy is located in the central area of

77   the Liguro-Provençal basin (Fig.1), where the dominant ocean currents are generally weak

78   (<20 cm s^{-1}) [Millot, 1999; Antoine et al., 2008b; Niewiadomska et al., 2008]. The main

79   processes that govern the pCO_2 variations at the sea surface on an annual scale, after removal

80   of the temperature effect, are vertical convective mixing and biological production [Begovic

81   and Copin-Montégut, 2002; Copin-Montégut al., 2004; Hood and Merlivat, 2001; Merlivat et

82   al., 2018]. Intense convection resulting from repeated high wind events in winter or early

83   spring when atmospheric temperatures are typically low brings nutrients to the surface layer

84   [Andersen and Prieur, 2000; Antoine et al., 2008b; Marty et al., 2002; Pasqueron de

85   Fommervault et al., 2015].

86   The objective of this study is to examine the impact of atmospheric forcing on surface

87   phytoplankton bloom initiation in the northwestern Mediterranean Sea. To this aim we use

88   concurrent hourly data of seawater carbon chemistry measured at depths less or equal to 10 m

89   at the BOUSSOLE mooring [Merlivat et al, 2018] and atmospheric flux measurements at the

90   Azur meteorological buoy 3.1 nm (5.8 km) away from BOUSSOLE in March and April 2016

91   to 2019. Additional measurements of phytoplankton chlorophyll-a (Chla), temperature and

92   density were provided by an underwater glider deployed in March-April 2016. The initiation

93   of biological carbon uptake is revealed by the sudden decrease in DIC measured at the

94   BOUSSOLE buoy.

95   In the Material and Methods section, we provide the description of data processing,

96   theoretical framework, and calculations used to evaluate mixing regimes in the water column

97   and net community production. The results section presents measured atmospheric and

98   biogeochemical parameters observed in March-April, and NCP estimates from 2016 to 2019.

99   The Discussion section relates our results to previous findings and presents our conclusions

100   regarding the drivers of phytoplankton bloom initiation.

101

102   2 Material and methods

103   2.1- Data from the BOUSSOLE mooring

104   CARIOCA sensors [Merlivat and Brault, 1995] installed on the BOUSSOLE buoy (43°22'N,

105   7°54'E; Fig.1) monitored hourly partial pressure, pCO_2, at both 3 and 10 m alongside salinity

106 and temperature (SEABIRD Scientific SBE 37 MicroCAT CTDs). Protocols for calibration of

107 in situ measurements are described in [Merlivat et al, 2018]. CARIOCA measurements of

108 pCO_2 and temperature are combined with total alkalinity (Alk) derived from salinity

109 [Merlivat et al., 2018] to calculate DIC. The dissociation constants of Mehrbach et al., (1973)

110 refitted by Dickson and Millero (1987) are used, as recommended by Alvarez et al. (2014) for

111 the Mediterranean Sea. For the March-April months mean salinity is 38.3, corresponding with

112 mean Alk equal to 2571.4 µmol kg^{-1} [Copin et al, 2004]. The expected precision of the

113 CARIOCA pCO_2, and DIC is 5 µatm, and 3 µmol kg^{-1}, respectively [Merlivat et al, 2018].

114 2.2- Glider observations

115 An iRobot Seaglider model 1KA (SG537) with an ogive fairing operated by the University of

116 East Anglia (UEA) [see Hemming et al., 2017] was deployed during the BOUSSOLE

117 monthly cruise (#169) [Golbol et al 2000] and recovered 1 month later with a ship of

118 opportunity. Diving to 1000 m, 147 dives were completed between March 7 and April 5 2016

119 repeatedly-sampling a square-shaped path surrounding the BOUSSOLE buoy (Fig. 1) with

120 corners pointing to cardinal directions. Out of 147 dives, a number of them contain data that

121 are within 10 km of the BOUSSOLE mooring, i.e. when it was sampling in the eastern corner

122 of the diamond path. The glider was equipped with a non-pumped SEABIRD Scientific SBE

123 9 CTD instrument package providing temperature and salinity, and a WET Labs Eco Puck

124 sensor providing relative phytoplankton Chla fluorescence, factory calibrated into Chla

125 concentration units (mg m^{-3}).

126 2.3- Azur meteorological buoy

127 The Azur meteorological buoy has been deployed since 1999 by the French weather forecast

128 Agency (Meteo-France) at 43°23'N, 7°50'E (Fig. 1). It provides hourly measurements of

129 surface wind speed extrapolated to 10 m height, U_{10} (m s^{-1}), net incoming and emitted long-

130 wave radiation, incoming short-wave radiation, and the sensible and latent heat fluxes. These

131 are needed to estimate the net air-sea heat budget at the sea surface (http://mistrals.sedoo.fr).

132 U_{10} is used to calculate wind stress, τ, as follows: $\tau = \rho_a\ C_d\ U_{10}^2$, where ρ_a is air density (1.2

133 kg m^{-3}), and C_d is the drag coefficient (1.4 x 10^{-3}). Photosynthetically Active Radiation (PAR,

134 mol photons $m^{-2}\ d^{-1}$) is related to solar irradiance (i.e. short-wave flux), SW, following PAR =

135 0.473 SW [Papaioannou et al., 1993].

136 2.4- Estimation of mixed and mixing layer depths

137 The mixing layer depth, Z_{mx}, is the upper part of a mixed layer of uniform density where
138 active turbulence occurs [Brainerd and Gregg 1995]. Several recent studies have highlighted
139 the significance of this layer to understand the phytoplankton phenology of phytoplankton
140 blooms [Brody and Lozier, 2015; Taylor and Ferrari, 2011]. Autonomous profiling floats
141 equipped with bio-optical sensors have also highlighted the importance of mixing rather than
142 mixed layers to characterize the onset and the development of a phytoplankton bloom. Wind-
143 driven and buoyancy-driven regimes control the characteristics and depth of active mixing
144 [Brody and Lozier, 2014, 2015, Ramuyantseva et al, 2015, Lacour et al, 2019, Pellichero et al,
145 2020]. Wind-driven mixing dominates in the presence of weak buoyancy forcing when heat
146 fluxes are small. In that case, the dominant mixing length scale is equal to the Ekman length
147 layer depth scale.

148 The daily mean mixed layer depth, Z_{ml} is derived for 2016 from glider vertical profiles of
149 temperature and salinity using the algorithm provided by Holte and Talley, (2009) estimated
150 using the potential density algorithm.

151 To estimate Z_{mx}, τ is used to calculate the Ekman layer depth, Z_{ek}, $Z_{ek} = \gamma\, u_*/f$, where γ is an
152 empirical constant (0.5), f is the Coriolis parameter (10^{-4} s^{-1}) over the BOUSSOLE area, and
153 u_* is the turbulent friction velocity, $u_* = \sqrt{\dfrac{\tau}{\rho_w}}$ (m s^{-1}), with ρ_w the density of the surface sea
154 water [Lacour et al, 2019]. When heat fluxes are large and positive, Enrikez and Taylor
155 (2015) proposed to express the mixing depth Z_{mx} in terms of the surface forcing, i.e. the
156 surface stress and a stabilizing surface buoyancy flux B_0, as follows:

157
$$\frac{1}{Z_{mx}^2} = \frac{f^2}{(C_3\ u_*)^2} + \frac{f\,B_0}{(C_4\ u_*^2)^2} \qquad (1)$$

158 With $C_3 = 1$, $C_4 = 0.57$, $B_0 = Q\,\lambda\,g\,/c_p\,\rho_0$, where Q is the net surface heat flux, λ the thermal
159 expansion coefficient (1.65 10^{-4} °C^{-1}), g the gravitational acceleration (9.81 m s^{-2}), c_p the
160 specific heat of water (4 10^{-3} J kg^{-1} °C^{-1}) and ρ_0 the pure water density (1000 kg m^{-3}).

161 2.5-Estimation of euphotic zone depth

162 The euphotic depth, Z_{eu}, is generally derived as the depth where PAR is 1% of its surface
163 value. Z_{eu} can be estimated from Chla at the surface using the method described by Lee et al.
164 (2007) based on the equation of Morel and Berthon (1989):

165
$$Z_{eu} = 34\ (Chla)^{-0.39} \qquad (2)$$

166 For the period between 2017 and 2019, GlobColour merged Chla products were used, which
167 are based on satellite observations with a resolution of 25 km, and a binning period of 8 days
168 (http://www.oceancolour.org). For 2016, glider surface Chla was used to derive Zeu instead
169 of satellite measurements. We excluded glider Chla between 05:00 and 20:00 UTC affected
170 by sunlight–induced fluorescence quenching, and we applied a depth-constant offset to glider
171 measurements using Chla water samples available on March 7.

172 2.6-Estimation of average mixing layer irradiance

173 We calculate the average mixing layer irradiance, I, function of the incident surface
174 irradiance, PAR, mixing layer depth, h, and the diffuse attenuation coefficient, K_d, estimated
175 from surface chlorophyll-a concentrations (Venables and Moore, 2010).

$$K_d = 0.05 + 0.057 \; Chla^{0.58}$$

176
$$I = \frac{PAR}{K_d h} (1 - e^{-K_d h}) \quad (3)$$

177

178 2.7 – Estimation of net community production

179 Biological Net Community Production rates, NCP (mmol m^{-2} day^{-1}), are calculated for
180 separate 3-day periods in March-April, 2016 to 2019 from DIC concentrations derived from
181 CARIOCA measurements, assuming that measurements in the top 10 m of the water column
182 are representative of an homogeneous mixing layer [Boutin and Merlivat, 2009; Merlivat et al,
183 2015; Pelicherro et al, 2020]. In the study area, current velocities are expected to be small
184 [Millot, 1999; Antoine et al., 2008; Niewiadomska et al., 2008], hence to estimate NCP, we
185 ascertain that the contribution of horizontal advection was negligible. Vertical mixing events
186 are identified by an increase in DIC resulting from upward movement of high DIC Levantine
187 Intermediate Water (LIW) at approximately 200 m depth [Copin-Montégut and Bégovic,
188 2002]. We isolated time periods when local physical processes were largely one-dimensional
189 in order to study changes in biological and chemical parameters that occurred during rapid
190 transitions from deep mixing to intermittent stratification. In 2016, over a four-day period,
191 March 18-21, the diurnal cycle of DIC values characterized by a maximum in the morning
192 followed by a minimum at the end of the day indicates the onset of organic matter formation.
193 The eddy diffusion term is negligible as the DIC gradient at the base of the mixing layer is
194 very weak, entrainment is not expected as changes in DIC are observed during periods of

195 stratification. For the identified periods, biological production and air-sea exchange are the

196 dominant processes responsible for daily changes in DIC.

197 NCP is thus estimated from temporal variation of the DIC integrated over Z_{mx} (DIC_{int}), and

198 corrected for the air-sea CO_2 flux contribution [Pelicherro et al, 2020]:

199 $$NCP = \left(\frac{\Delta DIC_{int}}{\Delta t}\right)_{bio} = \left(\frac{\Delta DIC_{int}}{\Delta t}\right)_{meas} - k \times s \times (pCO_{2atm} - pCO_{2sw}) \quad (4)$$

200 The first term in equation 4, $\left(\frac{\Delta DIC_{int}}{\Delta t}\right)_{meas}$, is the daily variation of DIC_{int} calculated over 3

201 days from the date identified as the start of phytoplankton bloom (t_0), whilst the remaining

202 part corresponds to DIC variability due to air-sea CO_2 exchange, where k is the gas transfer

203 velocity [Wanninkhof, 2014], s is the solubility of CO_2 in seawater [Weiss, 1974], and

204 pCO_{2sw} and pCO_{2atm} are respectively the partial pressures of CO_2, in μatm, in sea water and in

205 air [Merlivat et al, 2018].

206 3 Results

207 3.1- Description of the 2016 time-series
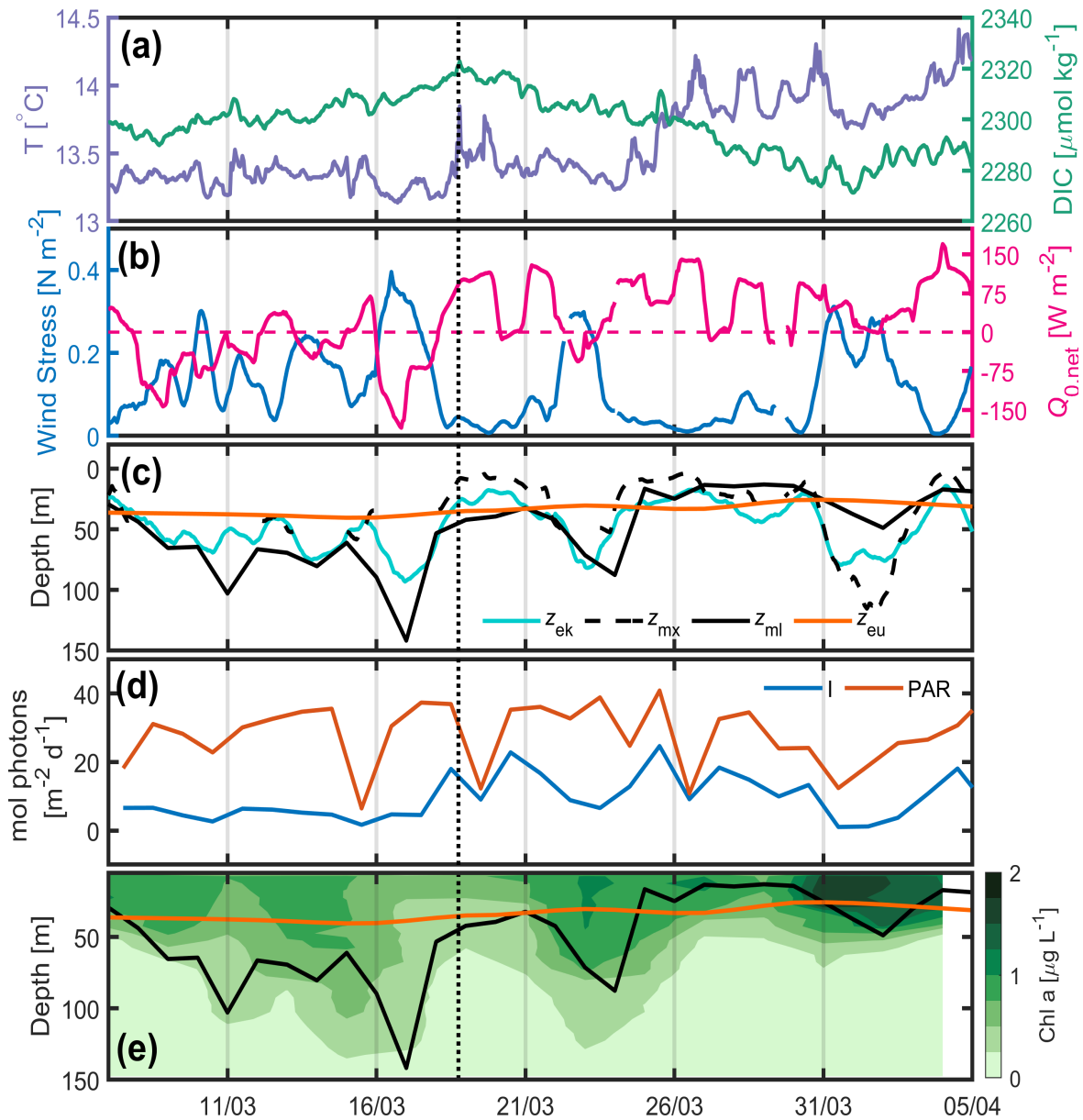
208

Figure 2. 2016 (a) Hourly DIC (green) and SST(purple) at the BOUSSOLE site, (b) hourly wind stress (blue) and net heat flux (pink) at the Azur buoy site. The pink dotted line indicates the change of sign of the net heat flux from negative to positive values, (c) daily depths of the mixed layer (black), mixing layer (dotted black), Ekman layer (cyan) and euphotic layer (orange) at the BOUSSOLE site. The black dotted line on panels (a), (b), (c) (d) and (e) indicates the onset time of the bloom (March 8). (d) PAR (orange) and I, average mixing layer irradiance (blue), (e) Glider-derived depths of the mixed layer (black curve, same as in (c)), euphotic layer (orange), and nighttime 2-day binned chlorophyll concentration (green coloring) retrieved between March 7 and April 5.

218   The temporal evolution of physical and biogeochemical parameters between March 7 and
219   April 5 2016 is displayed in Fig. 2. It shows an initial increase in DIC until March 18 (Fig.
220   2a), resulting from the vertical mixing of surface waters with the DIC-enriched underlying
221   LIW [Copin-Montégut and Bégovic, 2002], followed by a decrease in DIC that corresponds
222   to an increase of surface Chla (Fig 2e). Temperature increases intermittently over the same
223   time period (Fig. 2a), with a sharp increase on March 18 and 25. Before March 18 frequent
224   atmospheric fronts associated with wind forcing between 0.2 and 0.5 N m^{-2} were observed
225   (Fig. 2b). $Q_{0,net}$ was negative most of the time leading up to March 18, but mostly positive
226   afterwards (Fig. 2b). A clear anticorrelation was observed between τ and $Q_{0,net}$ (Fig. 2b). The
227   mixed-layer depth derived from the glider measurements (< 20 km away from the Boussole
228   site) deepened to > 70 m at times between March 8 and March 18, consistent with the passage
229   of frequent atmospheric fronts. From March 18 to April 5, Z_{ml} shoaled from ∼ 45 m to ~10 m,
230   excluding two short periods around March 24 and April 2 when atmospheric fronts were
231   passing (Fig. 2c). From March 18 to 31, Z_{mx} was for a considerable time either shallower than,
232   or at similar depth to Z_{ml} and Z_{eu} (Fig. 2c). The start of the increase in PAR from March 15
233   precedes the increase in irradiance by 3 days as a result of the decrease of the mixing layer
234   depth observed only after March 18 (Fig. 2d**).**

235   From March 18 to April 5, an increase in glider Chla was observed in the upper layer (Fig.
236   2e) as the result of the biomass accumulation within the water column following the initial
237   growth of surface phytoplankton [Behrenfeld, M. and E. Boss, 2014]. The same was observed
238   in the Southern Ocean [Pelicherro et al, 2019].

239   3.2- Description of the 2017-2018-2019 time-series

240   Only measurements at the BOUSSOLE and Azur buoys were available between 2017 and
241   2019. Here we focus on the periods between March 1 and April 25. In 2017, from March 9,
242   after the passage of a very active atmospheric front (τ up to 2.7 N m^{-2}), a decrease in DIC
243   accompanied by an increase in temperature was observed for a period of 14 days despite a
244   few short bursts of vertical mixing, typically lasting less than 1 day (Fig.3a, d, g). At the same
245   time, the net surface heat flux switched from negative to positive most of the time. Over this
246   14-day period, Z_{mx} was predominantly shallower than the Z_{eu} at times when DIC was
247   decreasing.

248   In 2018 (Fig. 3b, e, h) and 2019 (Fig. 3c, f, i), the weather records throughout the month of
249   March are very similar, showing a succession of very strong wind events at the start of the

investigated time periods, with τ values of up to 3.7 N m^{-2} and Z_{ek} values as deep as 300 m. On April 5, 2018, following a period of high wind stress resulting in the formation of a deep mixing layer (~250 m), a decrease in DIC and an increase in SST were observed over 3 days. At the same time, the net heat flux oscillated around zero. In 2019, CARIOCA data were only available after March 24. On March 30, 3 days after high winds, a decrease in DIC and an increase in temperature lasted 3 days, while simultaneously the net heat flux reversed from negative to positive.
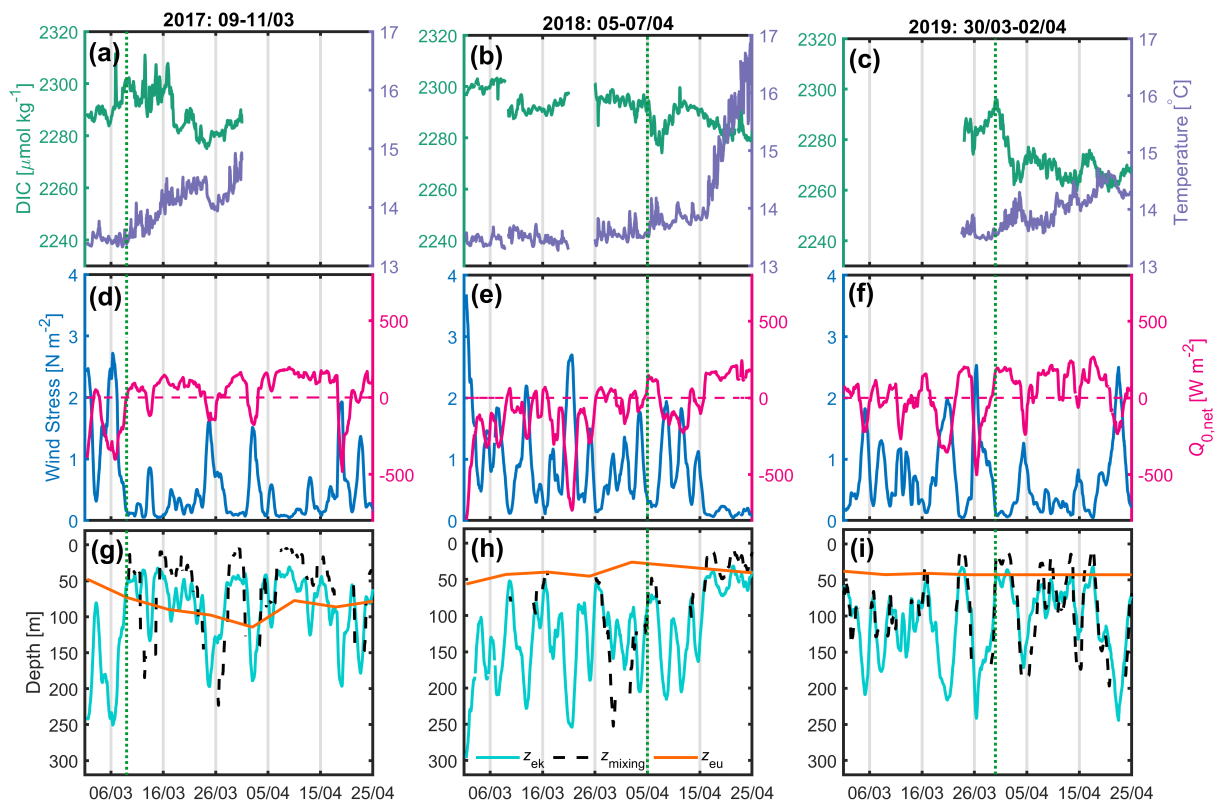
Figure 3. (a, b, c) 2017, 2018 and 2019 DIC (green) and SST (purple) at the BOUSSOLE site, (d, e, f) wind stress (blue) and net heat flux (red) at the Azur buoy site. (d, e, f) The red dotted line indicates the change of sign of the net heat flux from negative to positive values, (g, h, i) depths of the mixing layer (dotted black), Ekman layer (cyan) and euphotic layer (orange) at the BOUSSOLE site. The vertical dotted green line indicates the onset of the decrease of DIC.

For the period between 2017 and 2019, only satellite chlorophyll-a concentrations with a binning period of 8 days were available, which is too large to calculate the average mixing irradiance as it is highly variable on a daily scale (Fig 2.d).

267 3.3- NCP

268 NCP was estimated (Eq. 3) for 3-day periods over the four time-series between 2016 and

269 2019 (Table 1). Because we compute NCP only during periods when Z_{ml} and Z_{mx} shoal and

270 the air-sea CO_2 flux is very small, the measured total daily changes of DIC, dDIC/dt

271 (correlation coefficient, $r^{*2} > 0.70$), is expected to represent the biological consumption of

272 DIC. In 2016, 2017, and 2019, daily biological carbon uptake fluxes are between 38 and 191

273 mmol $m^{-2} d^{-1}$. PAR and I vary respectively from 30 to 53 and 13 to 25 mol photons m^{-2} d^{-1} for

274 the four considered periods (Table 2).

	T_0	dDIC/dt [a] $\mu mol\ kg^{-1}d^{-1}$	r^{*2} [b]	$\Delta DIC / \Delta t$ [c] $mmol\ m^{-2}d^{-1}$	r^{*2} [d]	air-sea flux CO_2 [e] $mmol\ m^{-2}d^{-1}$	NCP [f] $mmol\ m^{-2}\ d^{-1}$
2016 10m	March 18	-3.0	0.80	-37	0.68	1	38
2017 3m	March 9	-4.5	0.84	-188	0.86	3	191
2018 3m	April 5	-6.5	0.70			17	
2019 10m	March 30	-8.3	0.93	-163	0.63	4	167

275

276 Table 1. Net community production computed in the mixing layer over 3 days (NCP) after the

277 bloom onset (T_0). (a, b) variation of DIC at the measurement depth and linked correlation

278 coefficient; (c, d) change of integrated DIC over Z_{mx} and linked correlation coefficient ;(e)

279 CO_2 flux from the atmosphere to the ocean; (f), absolute value of calculated NCP is

280 considered in order to provide positive values throughout the presentation and discussion in

281 the manuscript.

282

283 4 Discussion

284 4.1 Analysis of the physical drivers of the bloom initiation over the 4 years, 2016-2019

285 4.1.1 In 2016, the consumption of carbon indicated by the decrease in DIC from March 18

286 attests the initiation of the formation of phytoplankton biomass (Fig. 2,). Between 2

287 successive days, March 17 and 18, a rapid decrease in daily wind stress from 0.24 to 0.04 N

288 m^{-2} results in a change of sign of the net heat flux from -68 to +56 W m^{-2} (Fig.4a) and a

289 shoaling Z_{mx}, which is for the most part shallower than Z_{eu} (Fig.4b) after March 18.

290
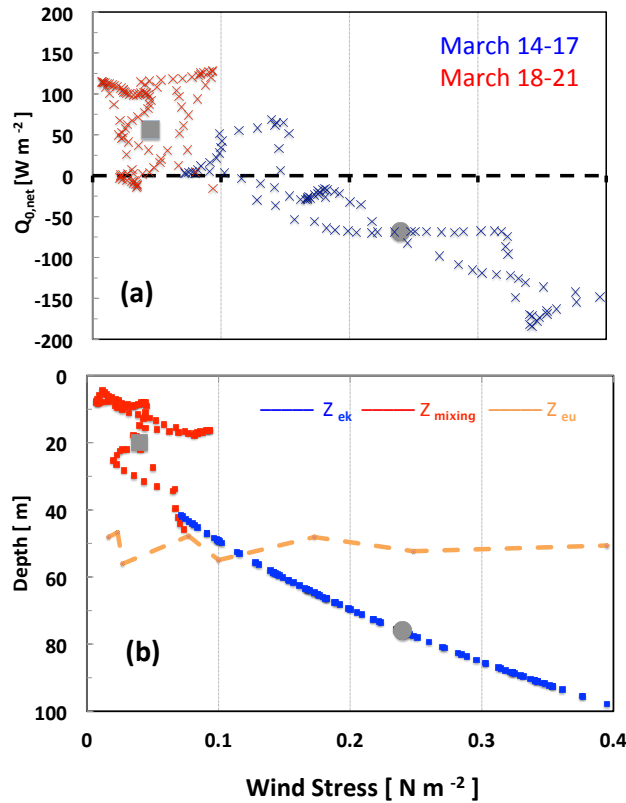
291 Figure 4. Changes of physical parameters (hourly values) at the onset of the 2016 bloom

292 during 2 consecutive periods of 4 days, March 14-17 (blue) and March 18-21 (red) as a

293 function of wind stress (a) net surface heat flux (b) depths of the Ekman, mixing and euphotic

294 layer. Grey circles and grey squares indicate mean values respectively on March 17 and

295 March 18. For comparison, the orange line shows the euphotic layer depth (March 14-21).

296 This illustrates the very fast change in heat flux and mixing layer thickness resulting from the

297 decrease in wind stress. The main drivers to explain the initiation of near surface spring

298 phytoplankton blooms proposed by [Taylor and Ferrari, 2011, Brody-Lozier, 2014, 2015] are

299 a decrease in wind strength, a positive surface heat flux, and a decrease in the dominant

300 mixing length scale. Our results indicate that a decrease in τ is a common component for these

301 last two mechanisms (Fig.4). The variability of $Q_{0,net}$ is strongly controlled by the variability

302 of the latent heat flux proportional to the wind speed. From March 17 to 18, the latent heat

303   flux changed by 84 W m^{-2} representing nearly 2 thirds of the total change of Q_0, with the

304   remainder originating from an increased short-wave flux. Hence, $Q_{0,net}$ increased as τ

305   decreased. In the same way Z_{mx}, which is related to τ and $Q_{0,net}$, decreased. This highlights the

306   major contribution of wind stress relaxation in controlling the net surface heat flux, and

307   subsequent stratification leading to sallower Z_{mx}

308   4.1.2 Over the 4 years, 2016-2019, during the months of March and April, at the very

309   beginning of spring, the conditions required for initiating the spring bloom are very similar

310   although the range of wind stress values is smaller in 2016 (Fig. 2, Fig. 3). The wind stress

311   values are low following storm events. For all years except 2018, Z_{mx} is smaller than Z_{eu}. The

312   average atmospheric and oceanographic conditions during the onset of the bloom are shown

313   in Table 2. The decrease of wind-driven mixing is then a dominant physical mechanism,

314   namely mixed layer shoaling which best predicts the timing of the spring bloom [Brody

315   Lozier, 2014, 2015]. Likewise, in the Southern Ocean, Pelicherro et al (2020) showed that a

316   bloom is initiated only when the wind-driven mixed layer decreases, even if the net heat flux

317   has been positive for some months.

318   4.2 DIC, Chla, Irradiance at the ocean surface in 2016

319   Between 18 and 21 March, a diurnal cycle in DIC is observed (Figure 5a) characterized by a

320   maximum in the morning followed by a minimum at the end of the day, indicating the onset

321   of organic matter formation. The decrease in DIC is accompanied by an increase of glider

322   surface Chla on 18 March and a simultaneous increase in the average mixing layer irradiance

323   (Fig. 5 b). It is worth noting that the Chla maximum does not occur until 31 March, 13 days

324   after the decrease in DIC. This maximum is the one identified in most cases by the Chla

325   satellite measurements with a binning period of 8 days. It follows that satellite data cannot

326   accurately characterize the conditions that prevail for the onset of a bloom, as these are

327   dictated by a great temporal variability of atmospheric forcings. Due to the seasonal

328   increase of surface irradiance in March-April, as well as the availability of nutrients following

329   vertical mixing with intermediate nutrient-enriched waters [Begovic and Copin-Montégut,

330   2002], the conditions for the onset of a bloom are met.

331

332
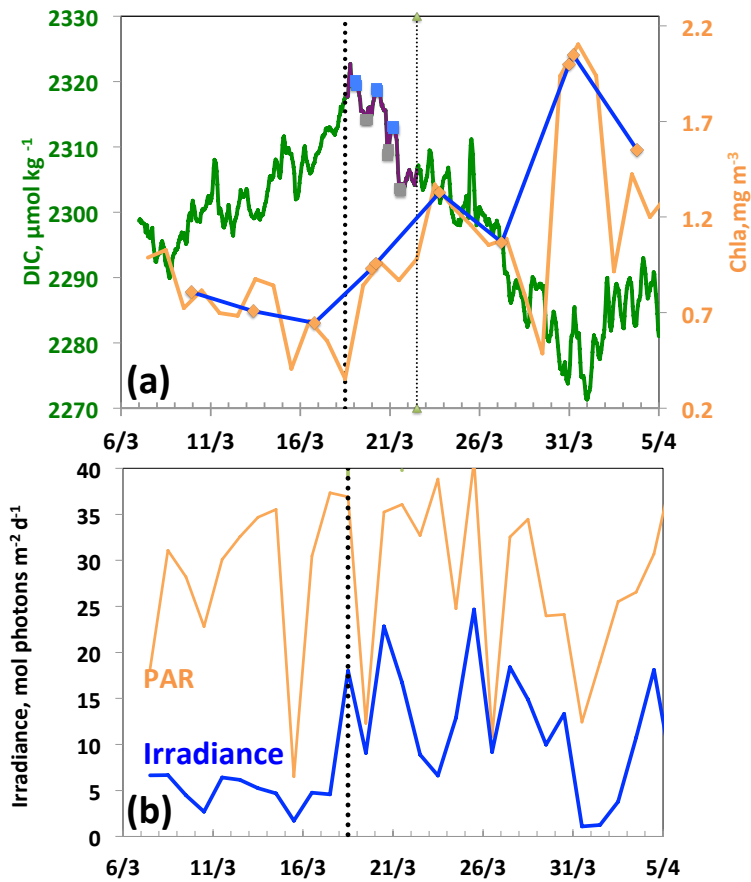
Figure 5. From March 7 to April 5, (a) DIC and Chla. The purple line and the squares (blue,morning; grey, evening) indicate the 3 days biological diurnal DIC changes during the period considered to compute NCP The blue and orange lines indicate the surface Chla when the glider was at a distance of less than 5 km (blue) and less than 20 km (orange) respectively from the Boussole buoy. (b) PAR and I average mixing layer irradiance. The vertical dotted black line indicates the onset of the bloom on March 18.

4.3- Biological carbon uptake

In 2016, 2017, and 2019, at the onset of the bloom Z_{mx} is shallower than Z_{eu} (Table 2). Two factors account for the observed large range of NCP variability at the time of triggering the bloom: dDIC/dt and Z_{ml}. In 2016 and 2017, DIC decreased over a period of 14 days, whereas it lasted for 3 days in 2018 and 2019, as a result of short-lived high wind events ($\tau > 1$ N m^{-2}). On April 2, 2018, a high surface phytoplankton Chla, 1.9 mg m^{-3}, was measured by satellite (Globcolour data) suggesting a strong biological signal. However, as Z_{eu} is significantly shallower than Z_{mx} (26 m vs. 65m; Fig. 3h), it would be incorrect to estimate NCP integrated over Z_{mx} using the DIC gradient measured at 3 m depth and likewise to compute the average mixing layer irradiance.

At the nearby DyFAMed site (Dynamique des Flux Atmospheriques en Mediterranee), using a 20-year O_2 time series, Coppola et al. (2018) estimated an annual net community carbon production equal to 7.1 mol m^{-2} yr^{-1}, or 19.4 mmol m^{-2} d^{-1}. Additionally, using determinations of primary production from ^{14}C in-situ incubations and of carbon export fluxes from sediment traps at DyFAMed, Marty and Chiaverini (2002) calculated average daily primary productions between 19.6 and 53 mmol m^{-2} d^{-1}. These estimates may have underestimated the annual NCP values as they were calculated from monthly observations while phytoplankton production varies on a daily timescale. Our DIC measurements highlight the large short-term variability of carbon consumption over a few days in March-April when bloom-triggering atmospheric conditions are met, such as a seasonal light increase and the availability of nutrients.

	T_0	Wind stress	Net heat flux	PAR	Z_{mixing}	$Z_{Euphotic}$	Irradiance
		N m^{-2}	W m^{-2}	mol photons m^{-2}d^{-1}	m	m	mol photons m^{-2}d^{-1}
2016	March 18	0.04 +/0.02	56+/-36	37+/-3	20+/-9	47	18
2017	March 9	0.12+/-0.02	45+/-21	30+/-3	28+/-12	71	13
2018	April 5	0.30+/-0.24	127+/-12	42+/-6	62+/-9	29	
2019	March 30	0.10+/-0.02	183+/-9	53+/-2	20+/-5	43	25

Table 2.   2016-2019.   Atmospheric drivers of the onset of the bloom: average values and standard deviation on the day of the start of the bloom, T_0.

5- Concluding remarks

Around March and April in the northwestern Mediterranean Sea, the seasonal change in lighting conditions and atmospheric forcing are the essential parameters that control the triggering of near-surface phytoplankton blooms. These mechanisms have been highlighted through the coupling of high-frequency physical and biogeochemical in situ observations. For years 2016 to 2019, a bloom started in March or early April identified by a decrease in surface DIC, following a period of intense mixing. The rapid decrease in surface wind speed entailed a switch from negative to positive air-sea net heat fluxes, essentially due to changes in the

latent air-sea heat flux proportional to wind speed. These analysis support the hypothesis that decreases in the depth of active mixing, a result of the transition from buoyancy-driven to wind-driven mixing, control the timing of the surface spring bloom.

We have shown that the onset of surface phytoplankton growth, identified in 2016 by a simultaneous initial decrease in DIC and an increase in surface Chla, precedes by a few days the surface chlorophyll maximum as detected by satellite measurements with a binning period of 8 days. This time span does not allow to identify precisely the contribution of atmospheric drivers to trigger the onset of the growth of phytoplankton as it occurs on a daily basis.

Data availability

BOUSSOLE data (2016-2019) are available in the SEANOE data base (Merlivat Liliane, Boutin Jacqueline (2020). Mediterranean Sea surface CO_2 partial pressure and temperature data. SEANOE. https://doi.org/10.17882/56709

Azur Meteorological buoy: http://mistrals.sedoo.fr

SChl, 8-day, 4 km x4 km resolution, level 3 mapped ocean color product distributed by the European Space Agency, available at http://www.ocean colour/org

All glider data is archived at the British Oceanographic Data Centre (BODC, https://www.bodc.ac.uk/data/bodc_database/gliders/).

Author contributions: VV and MG were respectively in charge of the BOUSSOLE mooring buoy maintenance and monthly water sampling. LB was responsible for the laboratory preparation and calibration of the CARIOCA sensors. GAL led the UEA glider mission in March-April 2016. DA and VV provided data and funding through the BOUSSOLE project and contributed to writing and editing of the manuscript.

The authors declare that they have no conflict of interest.

Acknowledgments: Michael Hemming was a PhD student at the University of East Anglia and Sorbonne University under the supervision of Prof. Jan Kaiser, Prof. Karen J. Heywood, Dr Dorothee Bakker and Dr Jacqueline Boutin, funded by the Defence, Science and

Technology Laboratory (Contract no. DSTLX1000092277) with cooperation with Direction Générale de l'Armement (DGA)-. The assistance of the UEA Glider Group in keeping the glider flying is also gratefully acknowledged. The BOUSSOLE time series project is funded by the Centre National d'Etudes Spatiales (CNES) and the European Space Agency (ESA/ESRIN contract 4000119096/17/I-BG). The authors acknowledge Météo-France for supplying the data from the Azur buoy and the HyMeX database teams (ESPRI/IPSL and SEDOO/Observatoire Midi-Pyrénées) for their help in accessing their data. Crew and Captains of R/V Tethys II are warmly thanked for assistance with operations at sea.

References

Álvarez, M., Sanleón-Bartolomé, H., Tanhua, T., Mintrop, L.,Luchetta, A., Cantoni, C., Schroeder, K., and Civitarese, G.: The CO2 system in the Mediterranean Sea: a basin wide perspective, Ocean Sci., 10, 69–92, https://doi.org/10.5194/os-10-69-2014,2014.

Andersen, V. and Prieur, L.: One-month study in the open NW Mediterranean Sea (DYNAPROC experiment, May 1995): Overview of hydrobiogeochemical structures and effects of wind events, Deep-Sea Res. I, 47, 397–422, 2000.

Antoine, D. M. Chami, H. Claustre, F. D'Ortenzio, A. Morel, G. Bécu, B. Gentili, F. Louis ,J. Ras, E. Roussier, A.J. Scott, D. Tailliez, S. B. Hooker, P. Guevel, J.-F. Desté, C. Dempsey and D. Adams. 2006, BOUSSOLE : a joint CNRS-INSU, ESA, CNES and NASA Ocean Color Calibration and Validation Activity. NASA Technical memorandum, N° TM-2006-214147, NASA/GSFC, Greenbelt, USA.

Antoine, D., P. Guevel, J.-F. Desté, G. Bécu, F. Louis, A.J. Scott and P. Bardey: The «BOUSSOLE» buoy; a new transparent-to-swell taut mooring dedicated to marine optics: design, tests and performance at sea, Journal of Atmospheric and Oceanic Technology, 25, 968-989, 2008a.

Antoine, D., F. d'Ortenzio, S. B. Hooker, G. Bécu, B. Gentili, D. Tailliez, and A. J. Scott: Assessment of uncertainty in the ocean reflectance determined by three satellite ocean color sensors (MERIS, SeaWiFS and MODIS-A) at an offshore site in the Mediterranean Sea (BOUSSOLE project), Journal of Geophysical Research, 113(C7), 2008b.

430   Begovic , M., and C. Copin-Montegut, Processes controlling annual variations in the partial

431   pressure of fCO2 in surface waters of the central northwestern Mediterranean sea (Dyfamed

432   site), Deep-Sea Research II, 49, 2031-2047, 2002

433   Behrenfeld, M. J, Abandoning Sverdrup's critical depth hypothesis on phytoplankton blooms.

434   Ecology, 91(4), 977-989, 2010

435   Behrenfeld, M. and E. Boss, Resurrecting the ecological underpinnings of ocean plankton

436   blooms. Annual Review of Marine Science, 6, 167-194, DOI: 10.1146/annurev-marine-

437   052913-021325, 2014

438   Brainerd, K. E., and Gregg, M. C, Surface mixed and mixing layer depths. Deep Sea Research

439   I: Oceanographic Research Papers, 42:1521–1543, 1995

440   Brody, S., and Lozier,M. Changes in dominant mixing length scale as a driver of

441   phytoplankton bloom initiation in the North Atlantic, Geophysical Research Letters 41, 3197–

442   3206, 2014.

443   Brody, S. R., & Lozier, M. S. , Characterizing upper-ocean mixing and its effect on the spring

444   phytoplankton bloom with in situ data. ICES Journal of Marine Science, 72(6), 1961-1970,

445   2015.

446   Chiswell, S. M.: Annual cycles and spring blooms in phytoplankton: don't abandon Sverdrup

447   completely. Marine Ecology Progress Series, 443, 39-50, 2011.

448   Copin-Montégut, C., Begovic, M.: Distributions of carbonate properties and oxygen along the

449   water column (0– 2000 m) in the central part of the NW Mediterranean Sea (Dyfamed site).

450   Influence of winter vertical mixing on air– sea CO2 and O2 exchanges. Deep-Sea Res., Part 2,

451   Top. Stud. Oceanogr. 49, 2049– 2066, 2002.

452   Copin-Montégut, C., M. Bégovic, and L. Merlivat.: Variability of the partial pressure of CO2

453   on diel to annual time scales in the Northwestern Mediterranean Sea, Mar Chem, 85(3-4),

454   169-189, 2004.

455   Coppola, L., Legendre, L., Lefevre, D., Prieur, L., Taillandier, V., & Riquier, E. D. :

456   Seasonal and inter–annual variations of dissolved oxygen in the northwestern Mediterranean

457   Sea (DYFAMED site). Progress in Oceanography, 2018.

458   Dickson, A. G., and F. J. Millero .: A comparison of the equilibrium constants for the

459   dissociation of carbonic acid in seawater media, Deep Sea Research Part A. Oceanographic

460   Research Papers, 34(10), 1733-1743 1987.

461   Enriquez, R.M., Taylor, J.R: Numerical simulations of the competition between wind-driven

462   mixing and surface heating in triggering spring phytoplankton blooms. ICES J. Mar. Sci. J. du

463   Cons. fsv071, 2015.

464   Golbol, M., Vellucci, V., Antoine, D .: BOUSSOLE, https://doi.org/10.18142/1, 2000.

465   Hemming, M. P., Kaiser, J., Heywood, K. J., Bakker, D. C., Boutin, J., Shitashima, K., Onken,

466   R. : Measuring pH variability using an experimental sensor on an underwater glider. Ocean

467   Science, 13 , 427–442,2017.

468   Holte, J., & Talley, L. : A new algorithm for finding mixed layer depths with applications to

469   Argo data and Subantarctic Mode Water formation. Journal of Atmospheric and Oceanic

470   Technology, 26(9), 1920-1939, 2009.

471   Hood, E. M., and L. Merlivat .: Annual and interannual variations of fCO2 in the

472   northwestern Mediterranean Sea: Results from hourly measurements made by CARIOCA

473   buoys, 1995-1997, J Mar Res, 59, 113-131, 2001.

474   Lacour, L., Briggs, N., Claustre, H., Ardyna, M., & Dall'Olmo, G.: The intraseasonal

475   dynamics of the mixed layer pump in the subpolar North Atlantic Ocean: A

476   Biogeochemical‐Argo float approach. Global Biogeochemical Cycles, 33(3), 266–281,2019.

477   Lee, Z., Weidemann, A., Kindle, J., Arnone, R., Carder, K. L., & Davis, C. : Euphotic

478   zone depth: Its derivation and implication to ocean-color remote sensing. Journal of

479   Geophysical Research: Oceans , 112 (C3),2007.

480   Mahadevan, A., D'asaro, E., Lee, C., & Perry, M. J. : Eddy-driven stratification initiates

481   North Atlantic spring phytoplankton blooms. Science, 337(6090), 54-58, 2012.

482   Marty, J.-C., Chiavérini, J. .: Seasonal and interannual variations in phytoplankton

483   production at DYFAMED time-series station, northwestern Mediterranean Sea. Deep

484   Sea Res. Part II 49, 2017–2030, 2002.

Mehrbach, C., C. H. Culberson, J. E. Hawley, and R. M. Pytkowicx .: Measurement of the apparent dissociation constants of carbonic acid in seawater at atmospheric pressure, Limnol Oceanogr, 18(6), 897-907, 1973.

Merlivat, L., and Brault, P.: CARIOCA BUOY, Carbon Dioxide Monitor, Sea Technol., 23–30, 1995.

Merlivat, L., Boutin, J., & Antoine, D. : Roles of biological and physical processes in driving seasonal air–sea CO 2 flux in the Southern Ocean: New insights from CARIOCA pCO 2. Journal of Marine Systems, 147, 9-20, 2015.

Merlivat, L., Boutin, J., Antoine, D., Beaumont, L., Golbol, M., & Vellucci, V. : Increase of dissolved inorganic carbon and decrease of pH in near surface waters of the Mediterranean Sea during the past two decades. Biogeosciences, 15(18), 5653-5662, 2018.

Millot: Circulation in the Western Mediterranean Sea, Journal of Marine Systems, 20, 423–442, 1999.

Morel, A., and J. F. Berthon . : Surface pigments, algal biomass profiles, and potential production of the euphotic layer: relationships reinvestigated in review of remote-sensing applications, Limnol. Oceanogr., 34, 1545–1562, 1989.

Niewiadomska, Katarzyna, Claustre, Hervé, Prieur, Louis, d'Ortenzio, Fabrizio, (2008), Submesoscale physical‐biogeochemical coupling across the Ligurian current (northwestern Mediterranean) using a bio‐optical glider, Limnology and Oceanography, 53, doi: 10.4319/lo.2008.53.5_part_2.2210.

Papaioannou, G., Papanikolaou, N., and Retalis, D. : Relationships of photosynthetically active radiation and shortwave irradiance. Theoretical and Applied Climatology, 48: 23–27, 1993.

Pasqueron de Fommervault, O., Migon, C., D'Ortenzio, F., Ribera d'Alcalà, M., and Coppola, L.: Temporal variability of nutrient concentrations in the northwestern Mediterranean sea (DYFAMED time-series station), Deep-Sea Res. Pt. I, 100, 1–12, 2015.

Pellichero, V., Boutin, J., Claustre, H., Merlivat, L., Sallée, J.-B., & Blain, S. : Relaxation of wind stress drives the abrupt onset of biological carbon uptake in the Kerguelen bloom: a multisensor approach. Geophysical Research Letters, 47, e2019GL085992

514   https://doi.org/10.1029/2019GL085992, 2020.

515   Rödenbeck, C., Keeling, R. F., Bakker, D. C. E., Metzl, N., Olsen, A., Sabine, C., and
516   Heimann, M.: Global surface-ocean pCO2 and sea–air CO2 flux variability from an
517   observation- driven ocean mixed-layer scheme, Ocean Sci., 9, 193–216, doi:10.5194/os-9-
518   193-2013, 2013.

519   Rumyantseva, A, Henson, S, Martin,A , Thompson, A. F, Damerell G.M, Kaiser J, Heywood,
520   K.J.: Phytoplankton spring bloom initiation: The impact of atmospheric forcing and light in
521   the temperate North Atlantic Ocean, Progress in Oceanography, 2019.

522   Siegel, D. A., S. C. Doney, and J. A. Yoder (2002), The North Atlantic spring phytoplankton
523   bloom and Sverdrup's critical depth hypothesis, Science, 296, 730– 733.

524   Sverdrup, H. U.: On vernal blooming of phytoplankton. Conseil Exp. Mer, 18, 287-295,1953.

525   Takahashi, T., Sutherland, S. C., Wanninkhof, R., Sweeney, C., Feely, R. A., Chipman, D. W.,
526   Hales, B., Friederich, G., Chavez, F., Sabine, C., Watson, A., Bakker, D. C. E., Schuster, U.,
527   Metzl, N., Yoshikawa-Inoue, H., Ishii, M., Midorikawa, T., Nojiri, Y., Kortzinger, A.,
528   Steinhoff, T., Hoppema, M., Olafsson, J., Arnarson, T. S., Tillbrook, B., Johannessen, T.and
529   Olsen, A., Bellerby, R., Wong, C. S., Delille, B., Bates, N. R., and de Baar, H. J. W.:
530   Climatological mean and decadal change in surface ocean pCO2 and net sea-air CO2 flux
531   over the global oceans, Deep-Sea Res. II, 56, 554–577, 2009.

532   Taylor, J. R., & Ferrari, R.: Shutdown of turbulent convection as a new criterion for the onset

533   of spring phytoplankton blooms. Limnology and Oceanography, 56(6), 2293-2307, 2011.

534   Venables, H. and Moore, C.M.: Phytoplankton and light limitation in the Southern Ocean:
535   Learning from high nutrient, high chlorophyll areas. Journal of Geophysical Research:
536   Oceans, 115(C2), 2010.

537   Wanninkhof, R.: Relationship between wind speed and gas exchange over the ocean revisited.
538   Limnology and Oceanography: Methods, 12(6), 351–362, 2014.

539   Weiss, R.: Carbon dioxide in water and seawater: the solubility of a non-ideal gas, Marine
540   chemistry , 2 (3), 203–215, 1974

541

543 Figures and tables

544 Figure 1. The area of the northwestern Mediterranean Sea showing the French and Italian
545 Rivieras, the island of Corsica, the main current branches (green arrows) in the Ligurian Sea
546 and the location of the BOUSSOLE buoy (white square) and the AZUR meteorological buoy
547 (yellow square). The black line indicates the glider's path in March-April 2016.

548 Figure 2. 2016 (a) Hourly DIC (green) and SST (purple) at the BOUSSOLE site, (b) hourly
549 wind stress (blue) and net heat flux (pink) at the Azur buoy site. The pink dotted line indicates
550 the change of sign of the net heat flux from negative to positive values, (c) daily depths of the
551 mixed layer (black), mixing layer (dotted black), Ekman layer (cyan) and euphotic layer
552 (orange) at the BOUSSOLE site. The black dotted line on panels (a), (b), (c) (d) and (e)
553 indicates the onset time of the bloom (18 March). (d) PAR (orange) and average mixing layer
554 irradiance (blue), (e) Glider-derived depths of the mixed layer (black curve, same as in (c)),
555 euphotic layer (orange), and nighttime 2-day binned chlorophyll concentration (green
556 coloring) retrieved between March 7 and April 5.

557 Figure 3. (a, b, c) 2017, 2018 and 2019 DIC (green) and SST (purple) at the BOUSSOLE site,
558 (d, e, f) wind stress (blue) and net heat flux (red) at the Azur buoy site. The red dotted line
559 indicates the change of sign of the net heat flux from negative to positive values, (g, h, i)
560 depths of the mixing layer (dotted black), Ekman layer (cyan) and euphotic layer (orange) at
561 the BOUSSOLE site. The vertical dotted green line indicates the onset of the bloom.

562 Figure 4. Changes of physical parameters (hourly values) at the onset of the 2016 bloom
563 during 2 consecutive periods of 4 days, March 14-17 (blue) and March 18-21 (red) as a
564 function of wind stress (a) net surface heat flux (b) depths of the Ekman, mixing and euphotic
565 layer. Grey circles and grey squares indicate mean values respectively on March 17 and
566 March 18. For comparison, the orange line shows the euphotic layer depth (March 14-21).

567 Figure 5. From March 7 to April 5, (a) DIC and Chla. The purple line and the squares
568 (blue,morning; grey, evening) indicate the 3 days biological diurnal DIC changes during the
569 period considered to compute NCP The blue and orange lines indicate the surface Chla when
570 the glider was at a distance of less than 5 km (blue) and less than 20 km (orange) respectively
571 from the BOUSSOLE buoy. (b) PAR and I average mixing layer irradiance. The vertical
572 dotted black line indicates the onset of the bloom on March 18.

573   Table 1. Net community production computed in the mixing layer over 3 days (NCP) after the

574   bloom onset (T_0). (a, b) variation of DIC at the measurement depth and linked correlation

575   coefficient; (c, d) change of integrated DIC over Z_{mx} and linked correlation coefficient ;(e)

576   CO_2 flux from the atmosphere to the ocean; (f), absolute value of calculated NCP is

577   considered in order to provide positive values throughout the presentation and discussion in

578   the manuscript.

579   Table 2. 2016-2019. Atmospheric drivers of the onset of the bloom: average values and

580   standard deviation on the day of the start of the bloom, T_0.

581